



Check for updates



# Design of Spiro-Substituted Phthalocyanine Hole-Selective Layers for Perovskite Solar Cells

<sup>1</sup>BCMaterials, Basque Center for Materials, Applications, and Nanostructures, UPV/EHU Science Park, Leioa, Spain | <sup>2</sup>Área de Química Orgánica, Instituto de Bioingeniería, Universidad Miguel Hernández, Elche, Spain | <sup>3</sup>Departamento de Química Inorgánica, Facultad de Ciencia y Tecnología, Universidad del País Vasco, UPV/EHU, Leioa, Spain | <sup>4</sup>Materials Physics Center, CSIC-UPV/EHU, Donostia - San Sebastian, Spain | <sup>5</sup>IKERBASQUE, Basque Foundation for Science, Bilbao, Spain

Correspondence: Ángela Sastre-Santos (asastre@umh.es) | Shahzada Ahmad (shahzada.ahmad@bcmaterials.net)

Received: 2 June 2025 | Revised: 21 July 2025 | Accepted: 27 July 2025

Funding: Spanish Ministry of Science and Innovation INTERACTION, Grant/Award Number: PID2021-129085OB-I00; Generalitat Valenciana, Grant/Award Numbers: CIPROM/2021/059 MFA/2022/028; Spanish Ministerio de Ciencia e Innovación/Agencia Estatal de Investigación, Grant/Award Number: PID2024-155430OB-I00

Keywords: hole-selective layers | perovskite solar cells | phthalocyanine | spiro cores

#### **ABSTRACT**

The design and development of hole-selective layers remain strategic for enhancing the performance and reliability of perovskite solar cells. We introduce phthalocyanines annelated with Spiro-core substituent at the  $\beta$  position as a molecular semiconductor to be employed as hole-selective layers. The placement of the Spiro unit improves the molecular packing, film uniformity, and energy level alignment, enhancing the hole extraction ability of the phthalocyanine and suppressing charge recombination at the perovskite/ hole-selective layer interface. Our findings highlight the symbiotic benefits of zinc phthalocyanine with Spiro substitution to deliver a power conversion efficiency of 18.91%, approaching the performance of Spiro-OMeTAD-based devices. This work opens the path of an innovative molecular design strategy and its potential with further optimization of the newly developed Spiro substitution in zinc phthalocyanines in perovskite solar cells.

# 1 | Introduction

Over the past decade, perovskite solar cells (PSCs) have emerged as a promising alternative to traditional silicon-based photovoltaics. This growing interest stems from their low material costs, simple processing methods, and competitive power conversion efficiencies (PCEs), without relying on a single material source and low materials usage [1, 2]. Despite these advances, the commercialization of PSCs faces challenges, including long-term stability, scalability, and environmental concerns related to material composition [3–5]. Addressing these issues is essential to enable the widespread production and adoption of PSC technologies.

The hole-transporting material (HTM) is one of the key components influencing the performance and stability of PSC [6–8] HTMs are responsible for efficiently extracting photogenerated holes from the valence band of perovskite and suppressing charge recombination at the perovskite/HTM interface by blocking electron injection, thereby enhancing photovoltaic performance and device durability [9, 10]. Substituting conventional HTMs such as Spiro-OMeTAD, poly[bis (4-phenyl) (2,5,6-trimethylphenyl)amine] (PTAA), and poly (3,4-ethylenedioxythiophene):polystyrene sulfonate (PEDOT:PSS) with cost-effective, efficient and durable HTM is prerequisite, as they suffer from UV degradation, phase separation (in the case of PEDOT:PSS), and

Mahdi Gassara and Lydia Ferrer equally contributed to this work.

This is an open access article under the terms of the Creative Commons Attribution License, which permits use, distribution and reproduction in any medium, provided the original work is properly cited.

© 2025 The Author(s). Solar RRL published by Wiley-VCH GmbH.

1 of 9

hydrophilicity, which compromise both stability and in some cases cost-effectiveness [10–13].

In this vein, small-molecule-based HTMs offer a rational design platform through molecular engineering to achieve enhanced performance and stability. Their opto-electrical properties can be tuned by selecting appropriate molecular cores and via side-arm engineering, leading to specific device requirements. Additionally, the formation of high-quality thin films with complete coverage and well-defined morphological and structural characteristics is paramount; this can be achieved through the incorporation of conjugated  $\pi$ -systems, which improve charge transport [14–17].

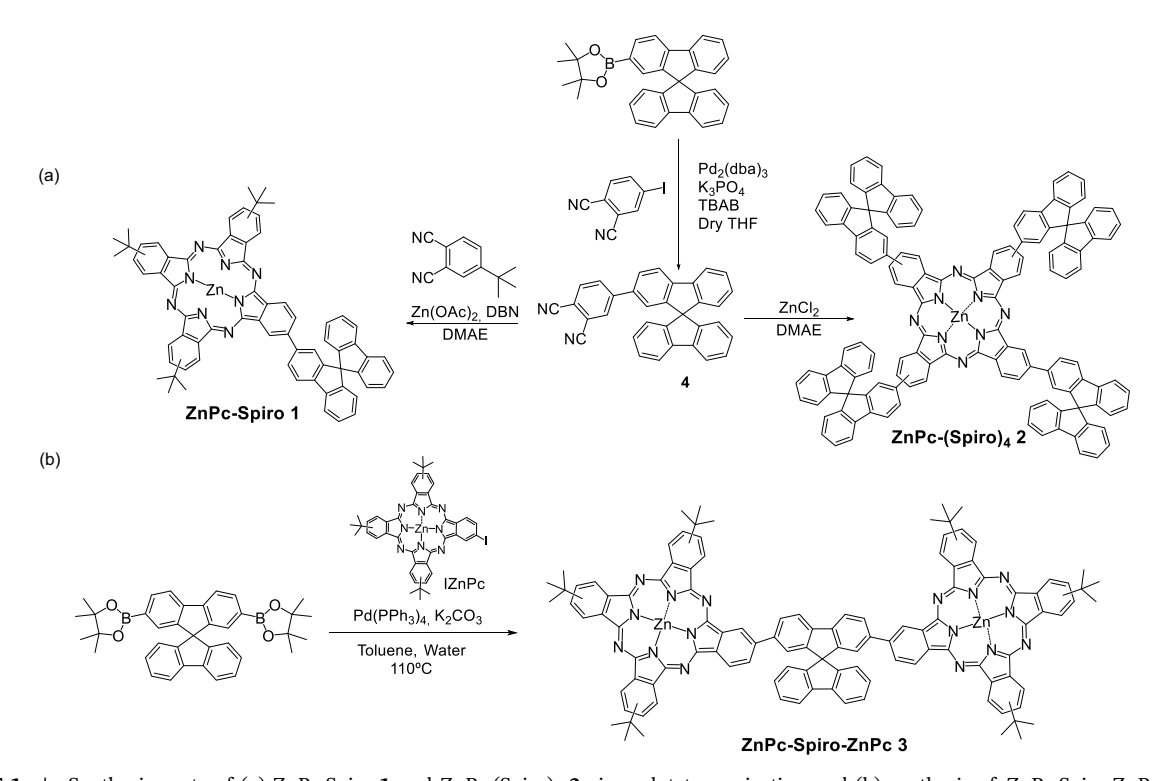
Among small molecules, phthalocyanines are aromatic heterocyclic compounds derived from porphyrins, representing a class of versatile  $\pi$ -conjugated molecules. It comprises four isoindole units bridged by nitrogen atoms, and their planar, extended  $\pi$ -system provides excellent thermal, chemical, and photostability [18, 19]. Phthalocyanines exhibit strong light absorption in the red and near-infrared regions, with characteristic Soret (B) and Q-bands, the latter reaching molar extinction coefficients up to 300,000 M<sup>-1</sup>·cm<sup>-1</sup> [20].

Recent advances in PSCs have been achieved with donor- $\pi$ -donor porphyrin structures, yielding PCEs up to 22.67% [21]. However, many of these systems still rely on dopants and additives such as lithium bis (trifluoromethanesulfonyl)imide (LiTFSI), cobalt complex, and *tert*-butylpyridine (*t*-BP) to boost hole mobility, which adversely affects long-term stability. To address this, redox-active phthalocyanine-based HTMs have been developed, achieving a PCE of 20.5% [22]. Further progress entails boosting internal electric fields through side-chain engineering-such as the introduction of methoxy, ethoxy groups,

which led to dopant-free HTMs with a PCE of 21.23% [23]. The incorporation of peripheral substituents into copper phthalocyanines resulted in a high PCE [24]. These results underscore the importance of side-chain tuning in porphyrins and phthalocyanines to modulate internal electric fields, improve charge transport, and achieve stable, efficient PSCs [25–30]. In our previous report, we developed ZnPc-based dimers as dopant-free HTMs for n-i-p type PSCs. A trimeric derivative with a central diketopyrrolopyrrole (DPP) unit flanked by two ZnPc as dopant-free HTM gave a competitive PCE (16.8%) [31]. Further, diethynyl-linked ZnPc dimers were introduced, including a Spirobifluorene-bridged dimer that outperformed Spiro-OMeTAD, endorsing the advantages of 3D molecular design [32].

Here, we highlight the innovative design of a series of Spirosubstituted zinc phthalocyanines (ZnPcs) through precise molecular engineering (Scheme 1), names as: ZnPc-Spiro (1), ZnPc-(Spiro)<sub>4</sub> (2), and the symmetrical ZnPc-Spiro-ZnPc (3), to uncover the role of Spiro motifs, offering tailored electronic and photophysical properties and their impact on photovoltaic properties of PSCs.

In most of the cases, for the hole extraction and transport process, the highest occupied molecular orbital (HOMO) level is favorable with respect to the perovskite valence band; however, the lowest unoccupied molecular orbital (LUMO) level is not energetically favorable and effective in preventing efficient back electron transfer and electron–hole recombination. Our developed phthalocyanine with Spiro-annelated possesses a substantially high-lying LUMO level, where ZnPc-(Spiro)<sub>4</sub> 2 exhibits the highest-lying LUMO. Arguably, this will help block the electron by collecting back-traveling electrons and will prevent losses arising from electron–hole recombination. This, in turn, increases the fill



SCHEME 1 | Synthesis route of (a) ZnPc-Spiro 1 and ZnPc-(Spiro)<sub>4</sub> 2 via cyclotetramerization and (b) synthesis of ZnPc-Spiro-ZnPc 3 through Suzuki-Miyaura coupling.

factor (FF) and the shunt resistance in the fabricated PSCs. We elected the Spiro core owing to its vital role as an HTM, and it features an orthogonal, nonplanar structure, consisting of two rigid aromatic systems joined at a central tetrahedral carbon. This geometry prevents  $\pi$ – $\pi$  stacking, reduces undesirable intermolecular charge recombination, and allows the formation of uniform, pinhole-free thin layers. The Spiro group helps to tailor the energy level of the HTM, facilitating effective hole extraction.

# 2 | Results and Discussion

The ZnPc-Spiro derivatives were synthesized through Suzuki-Miyaura coupling reactions and statistical cyclotetramerization [33] (Scheme 1). First, Spiro-phthalonitrile 4 was synthesized from 4-iodophthalonitrile [34] and previously synthesized 2- (9,9'-spirobi[fluoren]-2-yl)-4,4,5,5-tetramethyl-1,3,2-dioxaborolane [35] by a Suzuki-Miyaura reaction in the presence of Pd<sub>2</sub> (dba)<sub>3</sub>, K<sub>3</sub>PO<sub>4</sub> 1 M (aq), and TBAB, with 75% yield. ZnPc-Spiro 1 was obtained by cyclization of 4-tert-butyl phthalonitrile and Spiro-phthalonitrile 4 (3:1 ratio) in the presence of DMAE, DBU, and zinc acetate [Zn (OAc)<sub>2</sub>] (Yield = 30%). ZnPc-(Spiro)<sub>4</sub> was obtained by cyclization of Spiro-phthalonitrile 4 in the presence of ZnCl<sub>2</sub> and DMAE (Yield = 11%). Finally, we synthesized ZnPc-Spiro-ZnPc 3 via a Suzuki-Miyaura reaction through the coupling of iodophthalocyanine (IZnPc) [36] with the boronic diester [35], (Yield = 25%). All three molecules are characterized by spectroscopic techniques (<sup>1</sup>H-NMR and HR-MS). The details are provided in the supporting info (Figures S1-S11). The synthesized materials are partially soluble in common solvents but show high solubility in tetrahydrofuran (THF).

UV-vis absorption studies of the ZnPc-Spiro 1, ZnPc-(Spiro)<sub>4</sub> 2, and ZnPc-Spiro-ZnPc 3 compounds are measured in THF solutions (Figure 1a), and all the molecules exhibit the two characteristic bands of metallophthalocyanines. THF is a good solvent for these systems as the oxygen atom of the THF can coordinate with the Zn, avoiding  $\pi$ - $\pi$  interaction. The B band, or Soret band, appears between 300-400 nm, while the Q band, which is the more intense, appears between 550-750 nm, suggesting strong molecular packing and extended  $\pi$ - $\pi$  interaction. Further, the molecules with unbalanced Spiro core discourage molecular packing and show limited spectral band broadening, attesting to limited molecular packing. ZnPc-Spiro 1, ZnPc-(Spiro)<sub>4</sub> 2, and ZnPc-Spiro-ZnPc 3 present a maximum absorption rate within the Q band at 677, 691, and 676 nm, respectively. The Q band of ZnPc-Spiro-ZnPc 3 appears split due to the asymmetry caused by the presence of regioisomers, which is typical for this type of system [37]. Cyclic voltammetry experiments were conducted to estimate the HOMO and LUMO energy levels, assessing the potential of the designed ZnPc derivatives as HTMs in PSCs. The samples were measured in a 0.1 M TBAPF solution as the supporting electrolyte in THF. We use ferrocene/ ferrocenium (Fc/Fc<sup>+</sup>) redox couple as an external standard and elucidated the oxidation and reduction potentials of the molecules to calculate the values of HOMO and LUMO orbitals. The HOMO values for ZnPc-Spiro 1, ZnPc-(Spiro)<sub>4</sub> 2, and ZnPc-Spiro-ZnPc 3 are -4.95, -4.8, and -5.21 eV, respectively, compared to the valence band of the perovskite at -5.8 eV, which facilitates hole transport from the perovskite. On the other hand,

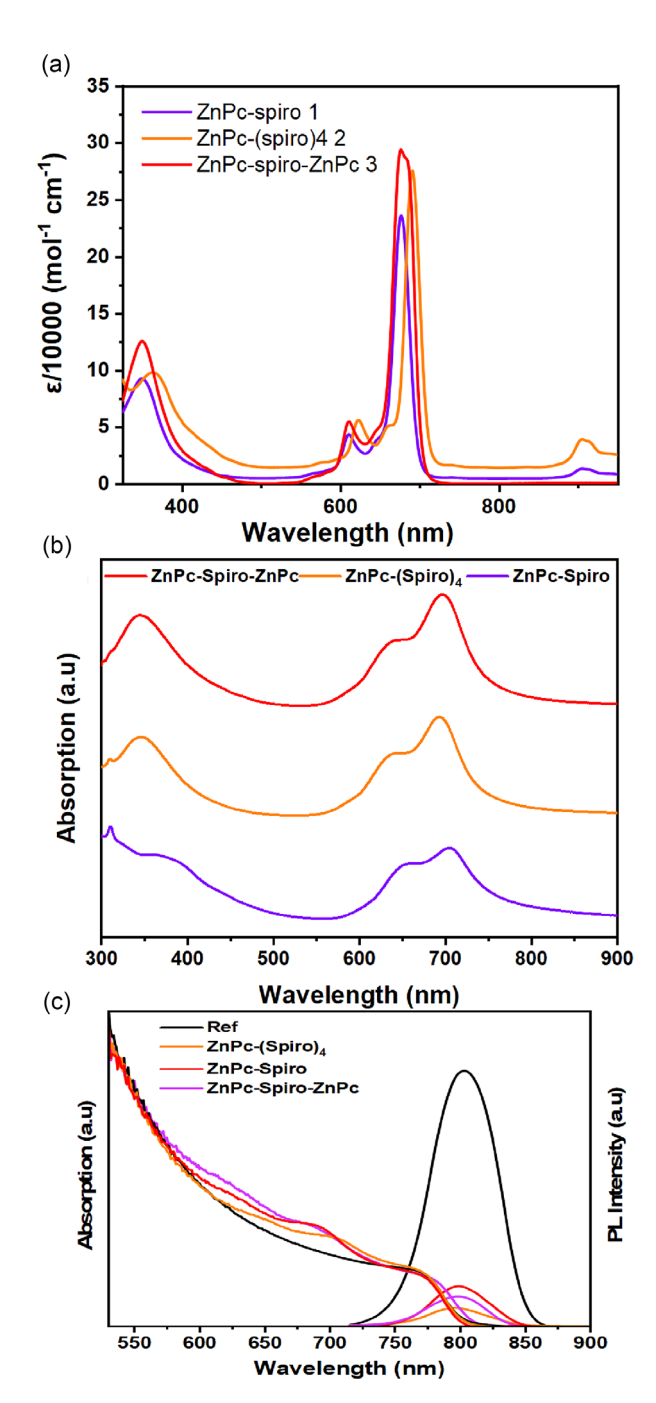


FIGURE 1 | Characterization of the ZnPc-Spiro 1, ZnPc-(Spiro)<sub>4</sub> 2, and ZnPc-Spiro-ZnPc 3 in THF via (a) UV-vis spectroscopy, (b) UV-vis absorbance of ZnPc-Spiro, ZnPc-(Spiro)4, and ZnPc-Spiro-ZnPc thin films, and (c) UV-vis-NIR absorbance and photoluminescence (PL) spectra of the perovskite with and without HTM's thin films.

the LUMO values are  $-3.51\,\mathrm{eV}$  for ZnPc-Spiro 1,  $-3.00\,\mathrm{eV}$  for ZnPc-(Spiro)<sub>4</sub> 2, and  $-3.25\,\mathrm{eV}$  for ZnPc-Spiro-ZnPc 3. By presenting a LUMO that is energetically higher than the perovskite ( $-3.9\,\mathrm{eV}$ ), these compounds prevent the flow of electrons from the perovskite to the HTM, thereby avoiding charge recombination. The high-lying LUMO level may act as a trap that collects all the back-traveling electrons.

The UV-vis absorption and emission profiles ZnPc-Spiro 1, ZnPc-(Spiro)<sub>4</sub> 2, and ZnPc-Spiro-ZnPc 3 thin films (Figure 1b) display

two characteristic absorption regions: a higher-energy band between 300-450 nm and a lower-energy band spanning 550–750 nm. These bands correspond to  $\pi$ – $\pi$ \* transitions, where the higher-energy B-band and broader Q-band arise from electronic excitations at distinct energy levels [31, 38]. To probe the impact of HTMs on the perovskite layer, ZnPc-Spiro 1, ZnPc-(Spiro)<sub>4</sub> 2, and ZnPc-Spiro-ZnPc 3 are deposited on top of the perovskite (Figure 1c). The changes arise primarily from the strong absorption of ZnPc itself, which overlaps with the perovskites absorption in the visible range. Additionally, the presence of ZnPc can influence the electronic environment of the perovskite, altering its absorption edge. We attribute this to the subtle structural changes at the interface [39]. The steadystate photoluminescence measurements (Figure 1c) of the thin film reveal the charge transfer dynamics at the perovskite/HTM interface, in its pristine form. Among them, ZnPc-(Spiro)<sub>4</sub> 2 displays the best photoluminescence quenching, suggesting its ability for effective hole extraction and transportation from the perovskite. In contrast, the ZnPc-Spiro 1 and ZnPc-Spiro-ZnPc 3 show comparatively weak photoluminescence quenching, signifying less efficient charge extraction. This enhanced quenching in ZnPc-(Spiro)<sub>4</sub> 2 is attributed to favorable energy level alignment and/or reduced interfacial recombination losses comparable to ZnPc-Spiro 1 and ZnPc-Spiro-ZnPc 3.

The designed HTMs are integrated into an n-i-p type device architecture with the structure FTO/b-TiO<sub>2</sub>/SnO<sub>2</sub>/perovskite/HTM/Au (Figure 2b). Formamidinium (FA)-rich,  $Cs_{0.05}FA_{0.9}MA_{0.05}PbI_3$  is used as a light harvester [31], and for phthalocyanines, we elected a concentration of 15 mM in chlorobenzene in contrast to 70 mM of Spiro-OMeTAD. The cross-sectional scanning electron microscopy (SEM) image validates the architecture used and displays the device stacks, and the thickness of the HTM layer is  $\approx$ 41.5 nm (Figure S10). Figure 3 compares the J-V curves of ZnPc-Spiro 1, ZnPc-(Spiro)<sub>4</sub> 2, and Spiro-ZnPc-Spiro 3 based PSCs with

Spiro-OMeTAD (control) devices; the detailed photovoltaic parameters are presented in Table 1. ZnPc-(Spiro)<sub>4</sub> 2 based PSCs measured a PCE of 18.91% ( $V_{OC} = 1049 \text{ mV}$ ,  $J_{SC} = 23.44 \text{ mA cm}^{-2}$ , FF = 76.87%) under AM 1.5G illumination, while ZnPc-Spiro 1 based PSCs measured a PCE of 14.22% ( $V_{\rm OC} = 917 \, {\rm mV}$ ,  $J_{SC} = 22.30 \text{ mA/cm}^{-2}$ , FF = 69.47%). Under similar conditions, the doped and additivated Spiro-OMeTAD-based gave a PCE of 21.05%. The measured voltage with ZnPcs suggests its band alignment, and the competitive performance of ZnPc-(Spiro)4 2 stems from its distinct molecular structure, which features four Spiro-linked ZnPc units, in contrast to the other HTMs that contain only one core group. Phthalocyanine molecules introduce deep traps that limit the fill factor mainly, and introducing Spiro annelated phthalocyanine can overcome this issue. Our design strategy not only increases the molecular size and rigidity but also helps to prevent aggregation and promotes uniform film formability. Spiro annelated phthalocyanine results in a highlying LUMO level, which blocks back-traveling electrons, thus decreasing leakage current and increasing shunt resistance and the FF. This is more pronounced in ZnPc-(Spiro)<sub>4</sub> 2, which displays higher PV performance than other molecules developed, as it is less rigid to allow improved molecular packing and more extensive  $\pi$ – $\pi$  interaction.

It is hypothesized that with a higher number of Spiro cores, ZnPc-(Spiro)<sub>4</sub> **2** will provide effective pathways for hole transport by creating a more interconnected 3D network. When doped with LiTFSI and t-BP, commonly used to enhance charge mobility and conductivity, these structural features become even more effective. The presence of multiple Spiro centers likely allows the dopants to interact more efficiently with the material, leading to better charge transport and improved overall device performance. Due to the bulky nature of the Spiro core, and for effective charge transport dopant is required for oxidation. We attribute these synergetic effects to ZnPc-(Spiro)<sub>4</sub> **2**, which

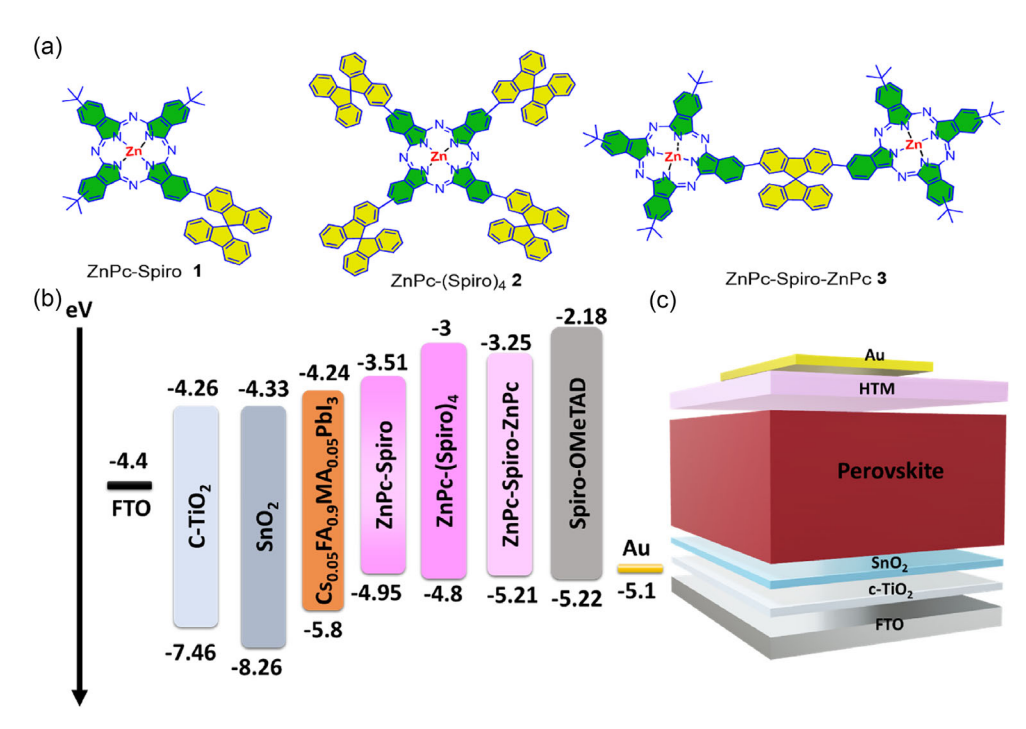
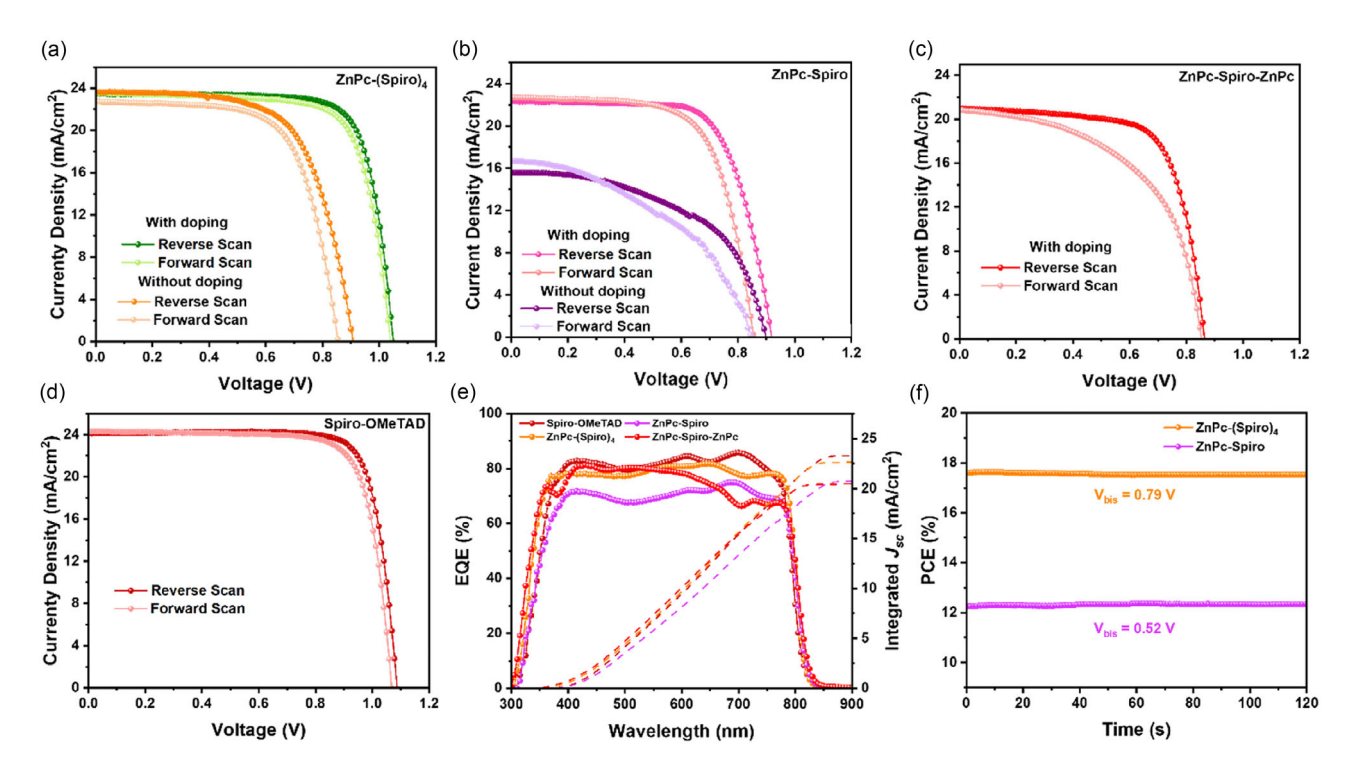


FIGURE 2 | (a) Molecular structure of the developed hole-selective layers, (b) energy level diagram, and (c) the device architecture employed.



**FIGURE 3** | (a) *J–V* curves of the ZnPc-(Spiro)<sub>4</sub> **2**, (b) *J–V* curves of the ZnPc-Spiro **1**, (c) *J–V* curves of the Spiro-ZnPc-Spiro based PSCs, (d) *J–V* characteristics of Spiro-OMeTAD, (e) IPCE spectra of the devices with ZnPc-Spiro, ZnPc-(Spiro)<sub>4</sub>, ZnPc-Spiro-ZnPc and Spiro-OMeTAD, and (f) steady-state power conversion efficiency (PCE) measured under maximum power point tracking for 120 s.

TABLE 1 | Photovoltaics parameters from the different HTMs developed in perovskite solar cells. Device statistics are presented for eight cells.

HTM's	Scan	V <sub>OC</sub> [mV]	$J_{\rm SC}~[{ m mA~cm}^{-2}]$	FF [%]	PCE [%]
ZnPc-(Spiro) <sub>4</sub> 2	Rs	1049	23.44	76.87	18.91
	Fs	1040	23.54	74.04	18.13
		$1024\pm25$	$23.36\pm0.18$	$75.38 \pm 1.49$	$18.06 \pm 0.85$
ZnPc-Spiro 1	Rs	917	22.30	69.47	14.22
	Fs	854	22.77	66.80	13.00
		$885\pm32$	$21.34 \pm 0.96$	$67.93 \pm 3.08$	$12.89 \pm 2.66$
ZnPc-Spiro-ZnPc 3	Rs	863	20.97	69.38	12.57
		$856\pm29$	$20.91 \pm 0.1$	$58.84 \pm 9.1$	$\textbf{10.83} \!\pm\!  \textbf{1.74}$
Spiro-OMeTAD	Rs	1086	24.11	80.35	21.05
	Fs	1075	24.74	78.40	20.86

outperforms the other HTMs studied, and Table 1 summarizes the parameters with the different ZnPc based HTMs. The PV parameters of the undoped ZnPc-Spiro 1 and ZnPc-(Spiro)<sub>4</sub> 2 are presented in Table S1, and notably, ZnPc-(Spiro)<sub>4</sub> 2 shows competitive performance even in the undoped state, significantly higher than Spiro-OMeTAD in its pristine form.

The external quantum efficiency (EQE) spectrum for the fabricated PSCs aligns with its integrated  $J_{\rm SC}$  (Figure 3e), both the control and Zn-PCs-based PSCs exhibit a similar trend, and the integrated  $J_{\rm SC}$  with control and ZnPc-(Spiro)<sub>4</sub> is 23.30 and 22.63 mA cm<sup>-2</sup>, respectively. In contrast, the ZnPc-Spiro system showed a lower EQE response with an IPCE value of 20.74 mA cm<sup>-2</sup>. Phthalocyanine shows absorption in the near

IR region, and thus may act as a co-light harvester, and in the EQE, a band edge for ZnPc-(Spiro)<sub>4</sub> **2** can be noted even after 800 nm. To further assess PSC performance, we monitored the stabilized PCE at the maximum power point under ambient conditions (50–60% humidity, 25°C with AM 1.5 G light illumination). The measured PCE values are consistent with the J-V curves measured, attesting to the reliability of the photovoltaic performance. To probe charge transport behavior, we measured the electrochemical impedance spectroscopy of the PSCs (Figure S11). The Nyquist plots for both systems displayed a single circular arc, corresponding to charge recombination resistance ( $R_{\rm rec}$ ) within the device [40]. The ZnPc-(Spiro)<sub>4</sub> **2** based PSCs gave a higher  $R_{\rm rec}$  (58.71  $\Omega$ ) compared to the control (0.11  $\Omega$ ) at an applied voltage of 750 mV, which follows the PV performance.

We uncovered the surface microstructure with SEM and atomic force microscopy (AFM) experiments (Figure 4). A uniform thin overlayer on the perovskite films can be noted for all ZnPc-Spiro, while it is thicker due to the higher concentration used in Spiro-OMeTAD (70 mM solution), compared to ZnPc-Spiro (15 mM), and can also be realized by the color contrast of the fabricated devices (Figure S12). These findings align with AFM imaging, which shows a reduction in grain boundaries and progressively lower root-mean-square (RMS) roughness values: 17.02 nm [(ZnPc-(Spiro)<sub>4</sub>], 17.4 nm (ZnPc-Spiro), and 17.72 nm (ZnPc-Spiro-ZnPc). The RMS roughness of ZnPc-based HTMs is almost similar, as compared to the Spiro-OMeTAD-based PSCs (11.91 nm). The reduced surface roughness of Spiro-OMeTAD stems from the higher concentration of Spiro-OMeTAD, which delivers a thick overlayer that smoothens the surface. The fourier transform infrared (FTIR) spectra was recorded to deduce the deposition of the ZnPc-(Spiro)<sub>4</sub> 2 layer on top of the FA-rich perovskite film (Figure S13). The FTIR spectra of ZnPc-(Spiro)<sub>4</sub> 2 shows several characteristic vibrational modes attributed to the phthalocyanine macrocycle and Spiro-functional groups. Notably, strong absorption bands appear in the range of 740-800 cm<sup>-1</sup>, corresponding to out-of-the-plane bending vibrations of aromatic C-H bonds, along with distinct bands between 1150 and 1300 cm<sup>-1</sup> related to C-N stretching and macrocyclic vibrations. Additionally, the aromatic ring stretching modes are observed in the region of 1450 - 1600 cm<sup>-1</sup>. These features serve as fingerprints for the ZnPc-(Spiro)<sub>4</sub> 2 (Table S2). In the FTIR of ZnPc-(Spiro)<sub>4</sub> 2 deposited on top of the perovskite layer, the characteristic bands remain detectable, albeit with reduced intensity, which is expected due to the low thickness of the layers as compared to the materials. The retention of these vibrational modes suggests the presence and structural preservation of ZnPc-(Spiro)<sub>4</sub> 2 on the perovskite surface. In contrast, the spectrum of the reference Spiro-OMeTAD shows distinct features, particularly the ether-related vibrations around  $\sim$ 1200–1300 cm<sup>-1</sup>, associated with its methoxy functional groups, further distinguishing the two HTMs. Overall, the results verify the presence of ZnPc-(Spiro)<sub>4</sub> 2 as a functional layer in the perovskite solar cell architecture.

X-band electron paramagnetic resonance (EPR) measurements at room temperature revealed narrow, isotropic signals in toluene of ZnPc-(Spiro)<sub>4</sub> **2**, ZnPc-Spiro **1**, and ZnPc-Spiro-ZnPc **3** with and without LiTFSI and *t*-BP doping (Figure 5a). The g-factor

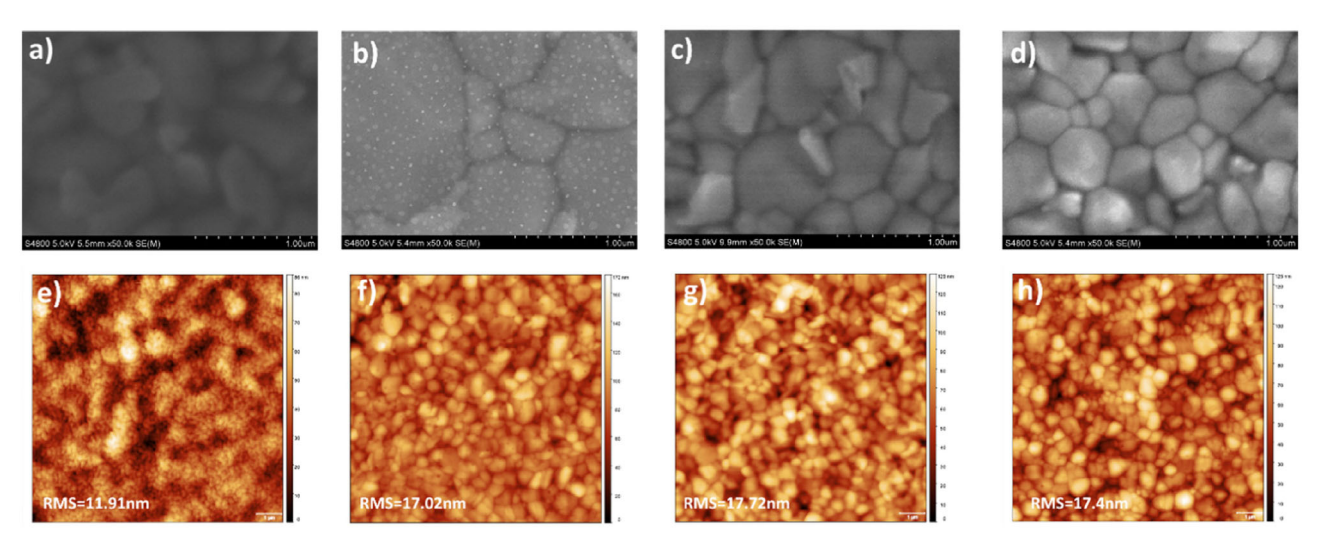
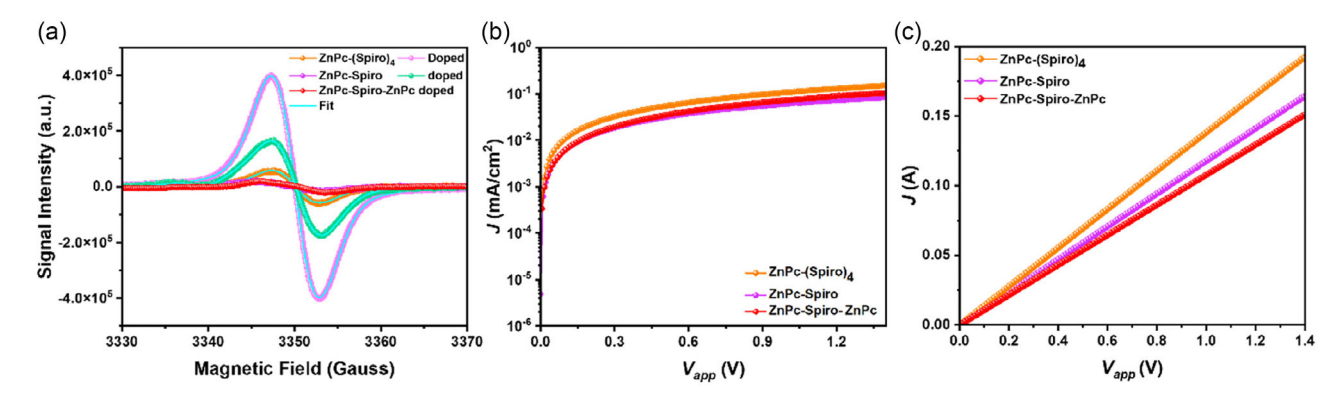


FIGURE 4 | Surface microstructure, SEM images of perovskite with (a) Spiro-OMeTAD, (b) ZnPc-(Spiro)<sub>4</sub> **2**, (c) ZnPc-Spiro **1**, (d) ZnPc-Spiro-ZnPc **3**, and AFM images of perovskite with (e) Spiro-OMeTAD, (f) ZnPc-(Spiro)<sub>4</sub> **2**, (g) ZnPc-Spiro **1**, and (h) ZnPc-Spiro-ZnPc **3**.



**FIGURE 5** | (a) Room-temperature EPR spectra registered on toluene solution ZnPc-(Spiro)<sub>4</sub> **2**, ZnPc-Spiro **1**, and ZnPc-Spiro-ZnPc **3**, (b) J–V curves for hole mobility measurements recorded in the FTO/PEDOT:PSS/HTM/Ag configuration, and (c) I–V curves for conductivity measurements obtained in the FTO/HTM/Ag configuration for the three different ZnPc-based HTMs.

values closely match with value of a free electron (2.0023). We determined the number of unpaired spins per milligram for each sample (Table 2) by referencing the EPR signal intensities against a copper sulfate standard. Notably, the undoped ZnPc-(Spiro)<sub>4</sub> 2 exhibited a substantially higher concentration of unpaired electrons or holes compared to the undoped ZnPc-Spiro by showing the lowest concentration. This variation is largely attributed to Spiro substitutions, which alter the local electronic environment and modulate spin density distribution within the ZnPc molecules. Importantly, upon doping, we noted an increase in EPR signal intensity, and this is more pronounced for ZnPc-(Spiro)<sub>4</sub> 2, indicating an effective generation of charge carriers. The multi-core Spiro architecture not only improves the intrinsic electronic properties of the HTM but also enhances its response to chemical doping. The higher density of oxidized species in ZnPc-(Spiro)<sub>4</sub> 2 will contribute to the hole conductivity, and this is in accordance with the photovoltaic performance measured.

We evaluated the charge carrier properties of the developed HTMs by estimating hole mobilities, and for this, we fabricated hole-only devices with a configuration ITO/PEDOT:PSS/HTM/Ag and calculated the mobilities using the Mott–Gurney equation [31]

$$J = \frac{9\varepsilon_{\rm r}\varepsilon_0\mu_{\rm h}V^2}{8L^3} \tag{1}$$

where J is the current density,  $\varepsilon_{\rm r}$  is the relative permittivity,  $\varepsilon_{\rm 0}$  is the permittivity of free space,  $\mu_{\rm h}$  is the hole mobility, V is the applied voltage, and L is the thickness of the HTM layer. The calculated hole mobility is noted to be  $5.68\times10^{-5}$ ,  $3.12\times10^{-5}$  and  $3.97\times10^{-5}$  cm²/V.s, for ZnPc-(Spiro)<sub>4</sub> **2**, ZnPc-Spiro **1**, and ZnPc-Spiro-ZnPc **3**, respectively. Similarly, we deduce the conductivity ( $\sigma$ ) value of the HTMs using the structure FTO/HTM/Ag, and the formula [31]

$$\sigma = \frac{JL}{VA} \tag{2}$$

where J is the current density, V is the applied voltage, L is the thickness of the HTM layer, and A is the active area of the device. By analyzing the J-V characteristics, the conductivity values noted to be  $1.8 \times 10^{-6}$ ,  $1.6 \times 10^{-6}$ , and  $1.5 \times 10^{-6}$  S cm<sup>-1</sup> for ZnPc-(Spiro)<sub>4</sub> **2**, ZnPc-Spiro **1**, and Spiro-ZnPc-Spiro **3**, respectively, providing insights into the charge transport efficiency of the HTM layers. ZnPc-(Spiro)<sub>4</sub> **2** exhibits higher electrical (hole

TABLE 2 | Best fit results of the EPR spectra.

HTMs	N (spin/mg)	g	ΔHpp (Gauss)
ZnPc-(Spiro) <sub>4</sub> 2	$2.3 \times 10^{14}$	2.0025	5.6
ZnPc-(Spiro) <sub>4</sub> <b>2</b> (doped)	$1.8 \times 10^{15}$	2.0024	5.6
ZnPc-Spiro 1	$1.2\times10^{14}$	2.0027	8.1
ZnPc-Spiro 1 (doped)	$7.4\times10^{14}$	2.0024	6.0
ZnPc-Spiro-ZnPc <b>3</b> (doped)	$6.5 \times 10^{13}$	2.0026	6.9

mobility and conductivity) merits among the three HTMs, and the charge transport characteristics are consistent with its higher EPR signal and photovoltaic performance. The multi-Spiro core structure of ZnPc-(Spiro)<sub>4</sub> **2** facilitates effective dopant interaction and charge carrier delocalization, contributing to faster and more efficient hole transport within the active layer.

#### 3 | Conclusion

With judicious molecular design, we developed Spiro-fuzed zinc phthalocyanine derivatives where at the  $\beta$ -position of the phthalocyanine core Spiro units are annelated. The number of Spiro substituents significantly impacts the electro-optical properties and device performance by modulating the electrical properties, spin density distribution, and solubility. Notably, ZnPc-(Spiro)<sub>4</sub> 2 exhibited higher concentrations of unpaired charge carriers. attributed to transformed electronic environments and boosted spin density localization. This is consistent with the fabricated solar cell performance, where ZnPc-(Spiro)<sub>4</sub> 2 gave competitive performance, not only due to elevated hole mobility and charge carrier density but also with the high solubility and uniformity as a layer, yielding a power conversion efficiency of 18.91%, which can be further pushed through optimization. Our results highlight that strategic Spiro functionalization in ZnPc derivatives serves as a pivotal factor in optimizing interfacial properties, device performance, and its potential for the development of solar cells by bridging molecular design with device efficiency, but also overcoming the two major challenges associated with solubility and band alignment through a symbiotic approach of the two cores.

# 4 | Experimental Section

# 4.1 | Materials

All chemicals were reagent grade, purchased from commercial sources, and were used as received unless otherwise specified. Some of the reactions were carried out in a microwave oven (CEM, Discover) equipped with a stirrer and pressure and temperature sensors. Column chromatography was performed on SiO<sub>2</sub> (40-63 μm) (Carlo Erba, Barcelona, Spain). TLC plates coated with SiO<sub>2</sub> 60F254 were visualized under UV light (Macherey-Nagel, Düren, Germany). <sup>1</sup>H and <sup>13</sup>C-NMR spectra were recorded at room temperature on a BRUKER AVANCE 400 spectrometer (Bruker, Billerica, MA, USA) (<sup>1</sup>H, 400 MHz) with chemical shifts (ppm) reported relative to the solvent peaks in the <sup>1</sup>H spectra. THF-d<sub>6</sub> was used as a deuterated solvent (Euroisotop, Saint-Aubin, France). Chemical shifts were reported in the  $\delta$  scale relative to TMS (0 ppm). NMR spectra are recorded at ambient probe temperature. UV-vis spectra were recorded with a Perkin Elmer Lambda 365 spectrophotometer in THF solution in the range of 250-800 nm. Fluorescence spectra were recorded with a HORIBA scientific SAS spectrophotometer in THF solution in the range 250-800 nm. High-resolution mass spectra were obtained from a Bruker Microflex matrix-assisted laser desorption/ionization time of flight (MALDI-TOF), using dithranol as a matrix. Spectra were measured with a Nicolet Impact 400D spectrophotometer.

# 4.2 | Synthesis of Molecule

# 4.2.1 | Synthesis of 4- (9,9'-sypirobi[fluoren]-2-yl) phthalonitrile 4

Into a 250 ml two-necked flask 2- (9.9'-spirobi[fluoren]-2-yl)–4,4,5,5-tetramethyl-1,3,2-dioxaborolane (1.92 g, 4.33 mmol), 4-iodophthalonitrile (1 g, 3. 90 mmol), Pd<sub>2</sub> (dba)<sub>3</sub> (90.2 mg, 0.19 mmol) and tetraoctylammonium bromide (118.5 mg, 0.22 mmol) were introduced under inert atmosphere. On the other hand, a degassed 0.5M aqueous solution of  $K_2PO_4$  (5.31 g, 25 mmol) was prepared. After degassing for 15 min, 100 ml THF was added while stirring, and then the 0.5M  $K_2PO_4$  degassed (during 15 min) solution was introduced. The temperature was raised to 100°C and left to react overnight. The crude was washed with 2 M HCl and water and extracted several times with ethyl acetate. Purification was achieved by chromatographic column with an eluent of hexane/dichloromethane in a 1:1 ratio. 1.7 g of a white solid (97%) was obtained.

<sup>1</sup>H-NMR (400 MHz, CDCl<sub>3</sub>) δ 7.99 (dd, J = 8.0, 0.6 Hz, 1H), 7.91 (ddt, J = 7.7, 4.9, 1.0 Hz, 3H), 7.85 (dd, J = 1.8, 0.7 Hz, 1H), 7.79 – 7.70 (m, 2H), 7.62 (dd, J = 8.0, 1.8 Hz, 1H), 7.42 (m, 3H), 7.21 – 7.10 (m, 3H), 6.94 (dd, J = 1.9, 0.6 Hz, 1H), 6.79 – 6.73 (m, 3H). <sup>13</sup>C NMR (101 MHz, CDCl<sub>3</sub>) δ 155.23, 149.70, 148.63, 147.24, 145.38, 142.87, 141.09, 139.66, 135.53, 132.97, 131.08, 130.50, 128.11, 127.39, 127.33, 127.29, 126.38, 123.48, 123.25, 121.92, 120.26, 119.86, 119.55, 115.49, 114.75, 114.64, 112.76, 107.43, 76.63, 76.52, 76.32, 76.00, 65.26, 55.68, 43.37, 30.85, 24.33, 21.92, 16.48, 13.39, 12.94, 10.71. HR-MS-MALDI-TOF: m/z calculated  $C_{31}H_{27}BO_2$  442.1422, obtained, 442.1416.

## 4.2.2 | Synthesis of ZnPc-Spiro 1

In a microwave tube, spiro-phthalonitrile (75 mg, 0.17 mmol), 4-*tert*-butylphthalonitrile (94.6 mg, 0.51 mmol), and zinc acetate (62.4 mg, 0.34 mmol) were introduced under an inert atmosphere. Subsequently, 0.35 ml of DMAE and one drop of DBN were added. The mixture was sonicated and degassed until completely dissolved. The microwave method employed was: 147°C, 200 W, 250 Ba, 1 hr. To purify, column chromatography was performed using hexane/dioxane as the eluent in a 2:1 ratio, and then, the product was washed with methanol and hexane, yielding 49 mg of dark green solid (30%).  $^1$ H-NMR (400 MHz, THF)  $\delta$  9.6–9.4 (m, 8H), 8.4–8.3 (s, 5H), 8.1–8.0 (m, 3H), 7.5–7.4 (m, 4H), 7.2–7.1 (m, 3H), 6.93 (m, 2H), 6.8–6.7 (m, 2H), 1.86 (m, 27H).  $\lambda$  max/nm (log  $\varepsilon$ ) 349 (4.97), 677 (5.37). HR-MS-MALDI-TOF: m/z calculated  $C_{69}H_{54}N_8Zn$ , 1058.3865, obtained, 1058.3862.

#### 4.2.3 | Synthesis of ZnPc-(Spiro)<sub>4</sub> 2

In a 5 ml two-neck round-bottom flask, spiro-phthalonitrile (75 mg, 0.17 mmol) and ZnCl $_2$  (11.92 mg, 0.09 mmol) were introduced, and a vacuum-argon purge was performed to create an inert atmosphere. Then, 400  $\mu$ L of DMAE was added, and the reaction mixture was degassed for 15 min. It was stirred overnight at reflux (144°C). Purification was carried out by column chromatography using chloroform/THF as the eluent in a 98:2 ratio. Finally, the product was washed with methanol and hexane

to obtain 25 mg of dark green solid (11%). <sup>1</sup>**H-NMR** (400 MHz, THF)  $\delta$  9.3–8.5 (m, 12 H), 8.4–7.7 (m, 25 H), 7.6–7.3 (m, 15 H), 7.3–7.1 (m, 10H) 7.0–6.8 (m, 7 H), 6.9–6.7 (m, 3H) 1.85 (m, 27H) **UV-vis (THF)**:  $\lambda$  max/nm (log  $\varepsilon$ ): 363 (4.99), 691 (5.44). **HR-MS-MALDI-TOF:** m/z calculated  $C_{132}H_{72}N_8Zn$  1832.3862, obtained 1832.3870.

#### 4.2.4 | Synthesis of ZnPc-Spiro-ZnPc 3

In a microwave tube, 2,2'-(spiro[fluorene-9,9'-fluorene]-2,7diyl)bis (4,4,5,5-tetramethyl-1,3,2-dioxaborolane) (29.55 mg, 0.05 mmol), zinc 2-iodo-6,16,23-tri-tert-butyl-phthalocyanate (100 mg, 0.12 mmol), Pd<sub>2</sub> (dba)<sub>3</sub> (2.65 mg, 0.003 mmol), and PPh<sub>3</sub> (6.085 mg, 0.02 mmol) and with tetrabutylammonium bromide (6.288 mg, 0.002 mmol) were introduced under argon. Subsequently, 2.3 ml of toluene was added, and the mixture was stirred for at least 30 min. Finally, 1.15 ml of a 2 M K<sub>2</sub>CO<sub>3</sub> solution was added, and the mixture was stirred and refluxed overnight. The product was purified by column chromatography on silica gel using hexane/dioxane (3:1) as the eluent, yielding 23 mg of dark green final product (25%). <sup>1</sup>H **NMR** (400 MHz, THF) δ 9.61–9.15 (m, 16H), 8.48 (s, 5H), 8.29 (m, 7H), 8.15 (m, 2H), 7.57 (s, 4H), 7.35 (m, 2H), 7.18 (m, 2H), 1.86 (s, 54H). **UV-vis (THF):**  $\lambda = \frac{1}{2} (\log \epsilon)$ : 349 (5.01), 676 (5.46). HR-MS-MALDI-TOF: m/z calculated  $C_{113}H_{92}N_{16}Zn_2$ , 1800.5633, obtained, 1800.5619.

#### Acknowledgements

This work received support from the Spanish Ministry of Science and Innovation INTERACTION {PID2021-1290850B-I00} and A.S.-S. thank the European Regional Development Fund "A Way to Make Europe" and the Spanish Ministerio de Ciencia e Innovación/ Agencia Estatal de Investigación (PID2024-155430OB-I00) and the Generalitat Valenciana (CIPROM/2021/059 and MFA/2022/028) for funding.

#### **Conflicts of Interest**

The authors declare no conflicts of interest.

#### **Data Availability Statement**

The data that support the findings of this study are available from the corresponding author upon reasonable request.

# References

- 1. Z. Yi, W. Wang, R. He, et al., Energy & Environmental Science 17 (2024): 202.
- 2. Y. Zheng, Y. Li, R. Zhuang, et al., Energy & Environmental Science 17 (2024): 1153.
- 3. P. Wang, Y. Wu, B. Cai, Q. Ma, X. Zheng, and W. H. Zhang, *Advanced Functional Materials* 29 (2019): 1807661.
- 4. S. Kazim, J. Huang, M. P. U. Haris, et al., Advanced Energy Materials 15 (2025): 2403248.
- 5. P. Zhu, C. Chen, J. Dai, et al., Advanced Materials 36 (2024): 2307357.
- 6. C. C. Zhang, K. Wei, J. Hu, et al., Materials Today 67 (2023): 518.
- 7. Y. Duan, Y. Chen, Y. Wu, Z. Liu, S. Liu, and Q. Peng, Advanced Functional Materials 34 (2024): 2315604.
- 8. J. Zhou, L. Tan, Y. Liu, et al., Joule 8 (2024): 1691.

- 9. W. Zhang, X. Guo, Z. Cui, et al., Advanced Materials 36 (2024): 2311025.
- 10. L. Zang, C. Zhao, X. Hu, J. Tao, S. Chen, and J. Chu, *Small* 20 (2024): 2400807
- 11. J. Luo, B. Liu, H. Yin, et al., Nature Communications 15 (2024): 2002.
- 12. X. Li, H. Yu, Z. Liu, et al., Nano-Micro Letters 15 (2023): 206.
- 13. A. Farokhi, H. Shahroosvand, G. Delle Monache, M. Pilkington, and
- M. K. Nazeeruddin, Chemical Society Reviews 51 (2022): 5974.
- 14. P. Murugan, T. Hu, X. Hu, and Y. Chen, *Journal of Materials Chemistry A* 10 (2022): 5044.
- 15. Q. Fu, Z. Xu, X. Tang, et al., ACS Energy Letters 6 (2021): 1521.
- 16. B. Wu, Q. Fu, L. Sun, et al., ACS Energy Letters 7 (2022): 2667.
- 17. W. Ling, F. Liu, Q. Li, and Z. Li, Journal of Materials Chemistry A 9 (2021): 18148.
- 18. E. Rezaee, D. Khan, S. Cai, et al., Materials Chemistry Frontiers 7 (2023): 1704.
- 19. D. Molina, J. Follana-Berná, and Á. Sastre-Santos, *Journal of Materials Chemistry C* 11 (2023): 7885.
- 20. N. Klipfel, J. Xia, P. Čulík, et al., Materials Today Energy 29 (2022): 101110.
- 21. C. L. Mai, Q. Xiong, X. Li, et al., Angewandte Chemie International Edition 134 (2022): e202209365.
- 22. J. Xia, J. Labella, P. K. Demircioglu, et al.,  $Solar\ RRL\ 8$  (2024): 2400371.
- 23. J. Cao, X. Lv, P. Zhang, et al., Advanced Materials 30 (2018):
- 24. Z. Yu, L. Wang, X. Mu, et al., Angewandte Chemie International Edition 60 (2021): 6294.
- 25. G. B. Xiao, X. Mu, Z. Y. Suo, X. Zhang, Z. Yu, and J. Cao, *Angewandte Chemie International Edition* 64 (2025): e202414249.
- 26. M. Haider, F. Mudasar, J. Yang, and S. Makarov, ACS Applied Materials & Interfaces 16 (2024): 49465.
- 27. G. Qu, L. Dong, Y. Qiao, et al., Advanced Functional Materials 32 (2022): 2206585.
- 28. M. Gassara, J. Garcés-Garcés, L. Lezama, et al., Journal of Materials Chemistry C 13 (2025): 1704.
- 29. Y. Ding, P. Xie, L. Zhang, et al., Advanced Functional Materials (2025): 2425443.
- 30. G. Qu, Y. Qiao, J. Zeng, et al., Nano Energy 118 (2023): 108974.
- 31. D. Molina, M. A. Ruiz-Preciado, B. Carlsen, et al., *ChemPhotoChem* 4 (2020): 307.
- 32. M. Pegu, D. Molina, M. J. Álvaro-Martins, et al., *Journal of Materials Chemistry C* 10 (2022): 11975.
- 33. A. Gouloumis, S.-G. Liu, A. Sastre, P. Vázquez, L. Echegoyen, and T. Torres, *Chemistry A European Journal* 6 (2000): 3600.
- 34. E. A. Krasnokutskaya, N. I. Semenischeva, V. D. Filimonov, and P. Knochel, *Synthesis* 1 (2007): 81.
- 35. T. Mujica-Fernaud, E. Montenegro, and J. Pfister, World Intellectual Property Organization International Bureau 2016, WO 2016/078738 A1.
- 36. A. Wang, L. Long, and C. Zhang, Tetrahedron 68 (2012): 2433.
- 37. E. Ortí, J. L. Brédas, and C. Clarisse, *Journal of Chemical Physics* 92 (1990): 1228.
- 38. Y. Liu, T. Xu, Z. Xu, et al., Advanced Materials 36 (2024): 2306982.
- 39. W. Li, W. Zhao, K. Li, and X. Han, Journal of Materials Chemistry C 12 (2024): 1147.

40. E. Ghahremanirad, O. Almora, S. Suresh, A. A. Drew, T. H. Chowdhury, and A. R. Uhl, *Advanced Energy Materials* 13 (2023): 2204370.

#### **Supporting Information**

Additional supporting information can be found online in the Supporting information section. Supporting Information Figure S1: 1H-NMR (400 MHz) spectrum of phthalonitrile 4 in CDCl<sub>2</sub> at 25°C. **Supporting Information Figure S2:** <sup>13</sup>C-NMR spectrum of phthalonitrile 4 in CDCl<sub>3</sub> as solvent at 25°C. Supporting Information Figure S3: (a) Positive mode HR MALDI-TOF mass spectroscopy of phthalonitrile 4, (b) theoretically calculated mass spectroscopy, and (c) experimental isotopic pattern. Supporting Information Figure S4: <sup>1</sup>H-NMR (400 MHz) spectrum of ZnPc-Spiro 1 in THF-d<sub>8</sub> at 25°C. Supporting Information Figure S5: (a) Positive mode HR MALDI-TOF mass spectroscopy of compound ZnPc-Spiro 1, (b) theoretically calculated mass spectroscopy, and (c) experimental isotopic pattern. Supporting Information Figure S6: <sup>1</sup>H-NMR (400 MHz) spectrum of ZnPc-(Spiro)<sub>4</sub> 2 in THF-d<sub>8</sub> at 25°C. Supporting Information Figure S7: (a) Positive mode HR MALDI-TOF mass spectroscopy of compound ZnPc (Spiro)<sub>4</sub> 2, (b) theoretically calculated mass spectroscopy, and (c) experimental isotopic pattern. Supporting Information Figure S8: <sup>1</sup>H-NMR (400 MHz) spectrum of ZnPc-Spiro-ZnPc **3** in THF-d<sub>8</sub> at 25°C. Supporting Information Figure S9: (a) Positive mode HR MALDI-TOF mass spectroscopy of compound ZnPc-Spiro-ZnPc 3, (b) theoretically calculated mass spectroscopy, and (c) experimental isotopic pattern. Supporting Information Figure S10: Cross-section image of fabricated PSCs with (a) Spiro-OMeTAD, (b) ZnPc-(Spiro)<sub>4</sub> 2, and (c) ZnPc-Spiro 1. Supporting Information Figure S11: Nyquist plots of PSCs under dark conditions at different voltages from 0.5 - 1.1 V for (a) Spiro-OMeTAD, (b) ZnPc-(Spiro)<sub>4</sub> 2, (c) ZnPc-Spiro 1, and interfacial charge recombination resistance extracted from Nyquist plots in the dark, (d) R<sub>ct</sub> and (e) R<sub>rec</sub> for Spiro-OMeTAD and ZnPc-Spiro<sub>4</sub>. Supporting Figure S12: Image of the fabricated PCs with (a) Spiro-ZnPc-spiro, (b) ZnPc-(spiro)<sub>4</sub>, (c) ZnPc-spiro, and (d) Spiro-OMeTAD. Supporting Information Figure S13: FTIR Spectrum of ZnPc-(Spiro)<sub>4</sub> 2, and ZnPc-(Spiro)<sub>4</sub> 2/perovskite, and Spiro/perovskite. Supporting Information Table S1: Photovoltaic parameters of pristine HTMs in PSCs. Supporting Information Table S2: Assignments of vibrational mode of ZnPc (Spiro)<sub>4</sub> 2, and of ZnPc-(Spiro)<sub>4</sub> 2/interface, and Spiro-OMeTAD/ perovskites.